Article

Gravitation-Based Edge Detection for Hyperspectral Images

Genyun Sun[1,2,3], Aizhu Zhang[1,2,*], Jinchang Ren[3], Jingsheng Ma[4], Peng Wang[1,2] and Yuanzhi Zhang[5]

[1] School of Geosciences, China University of Petroleum (East China), Qingdao, 266580, China; genyunsun@163.com (G.S.); wangpeng187@126.com (P.W.)
[2] Laboratory for Marine Mineral Resources Qingdao National Laboratory for Marine Science and Technology, Qingdao, 266071, China
[3] Department of Electronic and Electrical Engineering, University of Strathclyde, Glasgow, G1 1XQ, United Kingdom; jinchang.ren@strath.ac.uk
[4] Institute of Petroleum, Heriot-Watt University, Edinburgh, EH14 4AS, United Kingdom; jingsheng.ma@hw.ac.uk
[5] Key Lab of Lunar Science and Deep-exploration, Chinese Academy of Sciences, Beijing, 100012, China; yuanzhizhang@cuhk.edu.hk
* Correspondence: zhangaizhu789@163.com; Tel.: +86-532-86981952; Fax: +86-532-86981952

Abstract: Edge detection is one of the key issues in the field of computer vision and remote sensing image analysis. Although many different edge-detection methods have been proposed for gray-scale, color, and multispectral images, they still face difficulties when extracting edge features from hyperspectral images (HSIs) that contain a large number of bands with very narrow gap in the spectral domain. Inspired by the clustering characteristic of the gravitation, a novel edge-detection algorithm for HSIs is presented in this paper. In the proposed method, we first construct a joint feature space by combining the spatial and spectral features. Each pixel of HSI is assumed to be a celestial object in the joint feature space, which exerts gravitational force to each of its neighboring pixel. Accordingly, each object travels in the joint feature space until it reaches a stable equilibrium. At the equilibrium, the image is smoothed and the edges are enhanced, where the edge pixels can be easily distinguished by calculating the gravitational potential energy. The proposed edge-detection method is tested on several benchmark HSIs and the obtained results were compared with those of three state-of-the-art approaches. The experimental results confirm the efficacy of the proposed method.

Keywords: edge detection; hyperspectral image; gravitation; remote sensing; feature space

1. Introduction

The advent and growing availability of hyperspectral image (HSI) with both fine spectral and spatial resolution has opened the door to numerous new applications in remote sensing [1]. Hyperspectral sensors usually can capture hundreds of spectral bands simultaneously. Some famous hyperspectral imaging systems, such as AVIRIS (the Airborne Visible Infrared Imaging Spectrometer), HYDICE (the Hyperspectral Digital Imagery Collection Experiment), and EnMap (the Environmental Mapping and Analysis Program), can cover a range of 126-512 spectral bands with a spatial resolution from 3m to 30m per pixel. With such a high spatial resolution, the clearly depicted edges could be of great, interest in charactering the spatial structures of landscapes [2].

Over the past few decades, a large number of edge-detection techniques have been proposed, such as Canny [3], Marr [4], SUSAN (Univalue Segment Assimilating Nucleus) [5] and active contour based methods [6]. However, these approaches are designed primarily for gray, color or multispectral images and few studies have paid attention to edge detection on HSIs [7, 8]. In previous studies [8, 9], edge-detection tasks are completed by adapting color or multispectral approaches to hyperspectral images (HSIs). Accordingly, existing approaches for color or

multispectral based edge detection are discussed as follows.

In general, most approaches for color or multispectral based edge detection can be grouped into three categories: (1) monochromatic approaches, (2) vector based approaches and (3) feature-space based approaches. Monochromatic approaches combine all edge maps after applying well-established gray-scale edge detectors on each band, and typical rules for combining edges include the maximum rule [10], the summation rule [11] and the logic OR operation [12]. Although the fine spectral resolution of HSI provides invaluable and abundant information regarding the physical nature of different materials [8], edge features may be only observable over a small subset of bands in the HSI [13]. That is to say, different spectral bands may even contain inconsistent edges, which can easily leads to false edges by simple combination. To overcome this drawback caused by the combination rules, Lei and Fan combined the first principal component and hue component of color images to obtain complete object edges [14].

Different from monochromatic approaches, vector-based approaches consider each pixel as a spectral vector and then use vector operations to detect edges [15-22]. In these approaches, the gradient magnitude and direction are defined in a vector field by extending the gray-scale edge definition [9]. Di Zenzo's gradient operator [15], which uses the tensor gradient to define the edge magnitude and direction, is a widely used vector-based method. However, Di Zeno's method is sensitive to small changes in intensity because it is based on the measure of the squared local contrast variation of multispectral images. To overcome this problem, in Drewniok [17] Di Zeno's method is combined with the Canny edge detector with a Gaussian pre-filter model applied to each band for smoothing the image. Drewniok's method has better effectiveness, but it results in a localization error when the Gaussian scale parameter is large [23]. To remove both the effect of noise and the localization error caused by pre-filtering, a novel method based on robust color morphological gradient (RCMG) is proposed, where the edge strength of a pixel is defined as the maximum distance between any two pixels in its surrounding window [22]. The RCMG is robust to noise and helps top reserve accurate spatial structures due to a non-linear scheme is implied in the process [8].

Generally speaking, vector based approaches are superior to monochromatic approaches in multispectral edge detection due to their taking into consideration of the spectral correlation of the bands. Different from color images or multispectral images, however, HSIs usually consist of hundreds of contiguous spectral bands. Although the high spectral resolution of HSIs provides potential for more accurate identification of targets, it still suffers from three problems in edge detection. These include various interferences that lead to low homogeneity inside regions [24], spectral mixtures or edges that appear in a small subset of bands often cause weak edges [24] and inconsistent edges from narrow and abundant channels [25], which have made edge detection more challenging in HSIs. To tackle these challenges, it is necessary to consider the spatial relationships between spectral vectors [26]. As the approaches discussed above are based on computing a local variation of spectral vectors from a small surrounding window [25], it is inappropriate to directly extend them to HSIs.

Recently, many researchers have tried to develop feature-based new edge-detection methods because edge pixels have saliency in the feature space [27]. In Lin [27], color image edge detection is proposed based on a subspace classification in which multivariate features are utilized to determine edge pixels. In Dinh [25], MSI edge detection is achieved via clustering the gradient feature. The feature space is suitable to analyze HSIs because it is capable of showing data from various land cover types in groups [28]. In particular, a spatial-spectral jointed feature space, which takes into consideration both the spatial and spectral correlation between pixels, has attracted increasing attention [1, 26]. In addition to edge detection, feature space has also been widely used in other fields of image processing, such as hyperspectral feature selection [29, 30] and image segmentation [31, 32]. However, few studies focus on edge detection for HSIs using feature space.

Physical models that mimic real-world systems can be used to analyze complex scientific and engineering problems [31, 33, 34]. The ongoing research of physical models has motivated the exploration of new ways to handle image-processing tasks. As a typical physical model, Newton's law of universal gravitation [35] has received considerable attention, based on which, a series of image-processing algorithms has been proposed, such as the stochastic gravitational approach to

feature-based color image segmentation (SGISA) [31] and the gravitational collapse (CTCGC) approach for color texture classification [36]. Other gravitation model based approaches for classification include data gravitation classification (DGC) [37-39] and gravitational self-organizing maps (GSOM) [40]. The advantages of the gravity field model have inspired the development of new edge-detection method for gray-scale images [41, 42]. Although the image-processing procedure using gravitational theory is relatively easy for understanding, this theory is rarely used in edge detection for HSIs. As the gravitational theory describes the movements of objects in the three-dimensional feature space of the real world, we can easily extend it to n-dimensional feature space and apply it for edge detection in HSIs.

In this paper, a novel edge-detection method for HSIs based on gravitation (GEDHSI) is proposed. The main ideas of the proposed GEDHSI are as follows: (1) There exists a type of "force", called gravitation, between any two pixels in the feature space; (2) Computational gravitation obeys the law of gravitation in the physical world; (3) All pixels move in the feature space according to the law of motion until the stopping criteria are satisfied; then, the image system reaches a stable equilibrium; and (4) Finally the edge pixels and non-edge pixels are classified into two different clusters. Therefore, in the equilibrium system, edge responses can be obtained by computing the gravitational potential energy due to the relative positions. Different from our previous approach for gravitation based edge detection in gray-scale images [42], the proposed method features a dynamic scheme. By imitating the gravitational theory, all pixels move in the joint spatial-spectral feature space, which makes the GEDHSI more attractive and effective for HSIs. The experiment results illustrate both the efficiency and efficacy of the proposed method for HSI edge-detection problems.

The rest of the paper is organized as follows: The law of universal gravity is briefly reviewed in Section 2. The proposed gravitation-based edge detection method is presented in Section 3. The experimental validations of the proposed algorithm using both artificial and real HSIs are given in Section 4. Finally, the paper is concluded in Section 5.

2. Background of the Universal Law of Gravitation

According to gravitational theory [35], any two objects exert gravitational force onto each other. The forces between them are equal to each other but reverse in direction. The force is proportional to the product of the two masses and inversely proportional to the square of the distance between them, as shown in Eq. (1):

$$\vec{F}_{i,j} = G\frac{M_i M_j}{\left|\vec{Z}_i - \vec{Z}_j\right|^3}(\vec{Z}_i - \vec{Z}_j), \tag{1}$$

where $\vec{F}_{i,j}$ is the vector-form magnitude of the gravitational force between objects *i* and *j*, and their masses are denoted as M_i and M_j $(M_i < M_j)$, respectively. *G* is the universal gravitational constant, $\vec{Z}_i$ and $\vec{Z}_j$ represent the position vector of objects *i* and *j*. Newton's second law says that when a force, $\vec{F}_{i,j}$, is applied to object *i*, its acceleration, $\vec{a}_i$, depends only on the force and its mass, M_i.

$$\vec{a}_i = \frac{\vec{F}_{i,j}}{M_i}. \tag{2}$$

For M_i, two types of mass are defined in theoretical physics:

Gravitational mass, M_i^G, is a measure of the strength of the gravitational field due to a particular object. The gravitational field of an object with small gravitational mass is weaker than an object with larger gravitational mass.

Inertial mass, M_i^I, is a measure of an object's resistance to changing its state of motion when a force is applied. An object with large inertial mass changes its motion more slowly, and an object with small inertial mass changes it rapidly.

In physics, gravitational mass and inertial mass are usually treated as the same. In this paper, they are treated separately to enhance the adaptability of gravitational theory for HSI edge detection. That is to say, the gravitational force, $\vec{F}_{i,j}$, that acts on object *i* by object *j* is proportional to the product of the gravitational mass of objects *j* and *i* and inversely proportional to the square distance between them. $\vec{a}_i$ is proportional to $\vec{F}_{i,j}$ and inversely proportional to inertia mass of object *i*. More precisely, we rewrite Eqs. (1) and (2) as follows:

$$\vec{F}_{i,j} = G\frac{M_i^G M_j^G}{\left|\vec{Z}_i - \vec{Z}_j\right|^3}(\vec{Z}_i - \vec{Z}_j), \tag{3}$$

$$\vec{a}_i = \frac{\vec{F}_{i,j}}{M_i^I}, \tag{4}$$

where M_i^G and M_j^G represent the gravitational mass of objects *i* and *j*, respectively. M_i^I represents the inertial mass of object *i*.

The gravitational force obeys the superposition principle. Thus, for any object *k* in the space, the gravitational force exerted by objects *i* and *j* is calculated by Eq. (5).

$$\vec{F}_k = \vec{F}_{i,k} + \vec{F}_{j,k} = G\frac{M_i^G M_k^G}{\left|\vec{Z}_i - \vec{Z}_k\right|^3}(\vec{Z}_i - \vec{Z}_k) + G\frac{M_i^G M_k^G}{\left|\vec{Z}_j - \vec{Z}_k\right|^3}(\vec{Z}_j - \vec{Z}_k), \tag{5}$$

where $\vec{Z}_k$ is the position of object *k* in space Ω, and M_k^G is the gravitational mass of object *k*. The resultant force forms the gravitational field.

Because the gravitational field is conservative, there is a scalar potential energy (SPE) per unit mass at each point in the space associated within the gravitational fields. The SPE of object *i* exerted by object *j* is determined by Eq. (6) as follows:

$$\phi_{i,j} = -G\frac{M_i^G M_j^G}{\left|\vec{Z}_i - \vec{Z}_j\right|}, \tag{6}$$

Similar to the gravitational force, the SPE also obeys the superposition principle.

The SPE is closely linked with forces. It can be concluded that the force is the negative differential of the SPE [43], which is expressed as follows:

$$\vec{F}_{i,j} = -\nabla\phi_{i,j}, \tag{7}$$

where ∇ is the delta operator. The SPE function is extendable to high dimensional feature space and capable of reflecting the inhomogeneity of data, which is a key point for edge detection.

In gravitational systems, all objects move under the gravitational force until an equilibrium

phase is reached. In the equilibrium phase, all similar objects aggregate to form a cluster. Different clusters have different properties, such as SPE. Some gravitation-based algorithms are inspired from the characteristics of gravitational theory [31], [44]. In this paper, we assume that edge and non-edge pixels are by nature two different clusters. Therefore, they will have different SPEs. These properties constitute the background of the proposed method.

3. Gravitation-based Edge Detection for Hyperspectral Image (GEDHSI)

GEDHSI is a new edge-detection model based on Newton's law of universal gravitation. The proposed algorithm contains three phases, i.e. the mapping rule, traveling operator and SPE response. The mapping rule involves mapping HSI into a joint spatial-spectral feature space. The traveling operator is an iterative procedure in which all objects move in the feature space under the influence of gravitational force until the stopping criteria are met. When the traveling is stopped, we assume that the image system reaches a stable equilibrium. Therefore, the edge and non-edge pixels will have different SPEs in the equilibrium station due to the relative positions. Consequently, we can obtain the edge response by computing the SPE of each pixel to determine the edge map by setting an appropriate threshold as detailed below.

3.1. The Mapping Rule

The gravitational theory is derived from three-dimensional real-world space. To simulate the theory, we first map the HSI into a feature space. For a HSI denoted by $I^{H\times W\times B}$, the parameters H, W and B represent height, the width of the image and the number of bands, respectively. A simple feature space is composed only of its bands. This type of feature space primarily uses spectral information. To make full use of spatial and spectral information, inspired by [31], we define a spatial-spectral jointed feature space containing B+2 features (dimensions). In the feature space, each pixel addresses a location in the space:

$$\vec{Z}_i = (\vec{V}_i, \vec{S}_i) = (v_i^1, v_i^2 ..., v_i^b, \cdots, v_i^B, x_i, y_i), \text{ for } i=1, 2, \ldots, N, \tag{8}$$

where $N = H \times W$ is the total number of pixels in the image, $\vec{V}_i = (v_i^1, v_i^2, ..., v_i^B)$ is the spectral components of the pixel i, and $\vec{S}_i = (x_i, y_i)$ is its spatial position.

3.2 The Concepts of Gravitation

Once the joint spatial-spectral feature space is constructed, we can define some concepts of gravitation by analogizing with the gravitational theory.

Definition 1 (Object distance) The object distance $d_{i,j}$ between any two objects i and j is one dominant factor of their relationship. The distance measure $1/\left|\vec{Z}_i - \vec{Z}_j\right|$ as used in Eq. (1) will result in singularity. To avoid this problem and make $\frac{1}{d_{i,j}}$ smooth and finite, the distance is defined by Eq. (9), as follows:

$$d_{i,j} = 1 + \left(\frac{\left\|\vec{Z}_i - \vec{Z}_j\right\|}{\sigma}\right)^2, \tag{9}$$

where $\left\|\vec{Z}_i-\vec{Z}_j\right\|$ is the Euclidean distance between objects *i* and *j*, and σ is an influence factor. Need justify the effect of sigma here as how it may affect the distance and how to choose a suitable sigma et al

Definition 2 (Object SPE) For any two objects *i* and *j* in the feature space Ω, the SPE of object *i* produced by *j* is computed by substituting Eq. (9) into Eq. (6), as follows:

$$\phi_{i,j}=-G\frac{M_j^G M_i^G}{(1+(\left\|\vec{Z}_i-\vec{Z}_j\right\|/\sigma)^2)}, \tag{10}$$

where M_i^G and M_j^G are the gravitational mass of the objects *i* and *j*. In this paper, to simplify the calculation, gravitational mass of each object is set as a unit value.

Definition 3 (**Gravitational force**) The gravitational force describes the interaction of any two objects. According to Eq. (7), the gravitational force is proportional to the delta of SPE and along the decreased direction of SPE. Therefore, by substituting Eq. (10) into Eq. (7), we can obtain the gravitational force by

$$\vec{F}_{i,j}=-\nabla\phi_{i,j}=2G\frac{M_i^G\cdot \mathrm{M}_j^G}{\sigma}\cdot\frac{(\vec{Z}_j-\vec{Z}_i)}{(1+(\left\|\vec{Z}_i-\vec{Z}_j\right\|/\sigma)^2)^2}. \tag{11}$$

Gravitational force obeys the superposition principle. For a dataset *D*, which consists of *m* objects, the gravitational force of object *i* exerted by the dataset *D* is determined as the accumulated force for each objects within *D* as follows:

$$\vec{F}_i=\sum_{j\in D}2G\frac{M_i^G\cdot \mathrm{M}_j^G}{\sigma}\cdot\frac{(\vec{Z}_j-\vec{Z}_i)}{(1+(\left\|\vec{Z}_i-\vec{Z}_j\right\|/\sigma)^2)^2}. \qquad \text{v} \tag{12}$$

According to Eq. (12), the dataset *D* is a key factor for computing gravitational force. In general cases, all pixels are involved to compute the gravitational force. However, this will lead to high computational time. According to Eq. (12), the gravitational force attenuates toward zero when the distance increases. Thus, for objects that exceed a pre-specified range, we can safely assume that their gravitational forces are zero to simplify the computation.

To this end, the dataset *D* can be constructed by

$$D=\left\{ j \left| \left\|\vec{S}_i-\vec{S}_j\right\|< r \text{ and } \left\|\vec{V}_i-\vec{V}_j\right\|<\delta \right.\right\}, \tag{13}$$

where *r* is the radius of a local circular window in the spatial domain, δ is the radius in the spectral domain, and *j* is the neighbor pixel around the object *i*. *r* and δ construct a local suprasphere in the feature space. Here, to balance the effect of the spatial and spectral distance, the position of each object is stretched in spectral domain by $\vec{V}_i'=\vec{V}_i.\frac{r}{\delta}$. Thus, the influence factor σ is equal to r, and $\vec{Z}_i$ is replaced by $\vec{Z}_i=(\vec{V}_i',\vec{S}_i)$. All objects inside the suprasphere compose the dataset *D*.

Under the resultant force, all objects will travel in the feature space. According to Eq. (4), in addition to resultant force, inertial mass is critical in the traveling procedure. The definition of inertial mass is given below.

Definition 4 (**Inertial mass**) According to Eq. (3), inertial mass is necessary when calculating acceleration. Inertial mass is defined as follows:

$$M_i^I = \sum_{j \in D} \exp(-(\frac{\left\| \vec{Z}_j - \vec{Z}_i \right\|}{\sigma})^2), \tag{14}$$

Inertial mass is capable of capturing the local information with self-adaptation when traveling.

3.3 Traveling Operator

In the traveling stage, all objects move step by step in the feature space under the gravitational force until the stopping criteria are met. To compute the step size at iteration *t*, the acceleration is first computed according to Eq. (15), followed by calculation of the step size using the law of motion (Eq. (16)). Finally, the position is updated using Eq. (17):

$$\vec{a}_i(t) = \frac{\vec{F}_i(t)}{M_i^I(t)}, \tag{15}$$

$$\Delta \vec{Z}_i(t) = \frac{1}{2}\vec{a}_i(t)\Delta t^2 + \vec{v}_i(t)\Delta t, \tag{16}$$

$$\vec{Z}_i(t+1) = \vec{Z}_i(t) + \Delta \vec{Z}_i(t), \tag{17}$$

where $\vec{v}_i(t)$ is the velocity of object *i* at time *t*. To make the object move directly toward the potential center, $\vec{v}_i(t)$ is considered zero in Δt time. $\vec{F}_i(t)$ and $M_i^I(t)$ are obtained using Eq. (12) and Eq. (14), respectively. Δt is the time interval in two adjacent iterations and is set to 1. Thus, Eq. (17) is replaced by Eq. (18):

$$\vec{Z}_i(t+1) = \vec{Z}_i(t) + \frac{1}{2}\vec{a}_i(t) = \vec{Z}_i(t) + \frac{\vec{F}(t)}{2M_i^I(t)}. \tag{18}$$

The traveling operator is an iterative procedure, and the operator will be repeated until the following stopping criteria are met: (1) The minimum step size $\varepsilon < 0.001$, or (2) the iterations reach a maximum *T*=20. In this stage, each pixel moves along the direction of the associated gravitational force. By traveling, they can find other, similar pixels, which remove the influence of noise and preserves the structural detail.

3.4 SPE Response

When the traveling stops, the image system reaches a stable equilibrium where similar objects will cluster together. Due to the relative positions, different objects have various SPEs. The SPE of each pixel can be calculated. For edge pixels, the SPE is relatively high, whereas for non-edge pixels, the SPE is relatively low. Thus, we take the SPE of each pixel as the edge response. The calculation of the SPE of each object is also restricted to the dataset D and using Eq. (19).

$$\Phi_i = \sum_{j \in D} \varphi_{i,j} = \sum_{j \in D} -G \frac{M_j^G M_i^G}{(1 + (\left\| \vec{Z}_i - \vec{Z}_j \right\| / \sigma)^2)}. \tag{19}$$

Figure 1 (a) is a HSI obtained by AVIRIS that has 224 bands and contains four different regions (part of the Farmland image shown in Figure 9(b)). There is high heterogeneity within the same region, and the edges at transitional regions are ambiguous and hard to distinguish. The SPE map (Figure 1 (b)) is rather smooth within the same regions and steep at the transitions. Figure 1 (c) is the three-dimensional display of Figure 1 (b), from which we can find that there are no peaks within the same regions, and the SPE is steep at the boundary. Thus, it is easy to select an appropriate

threshold to separate the edge and non-edge pixels.

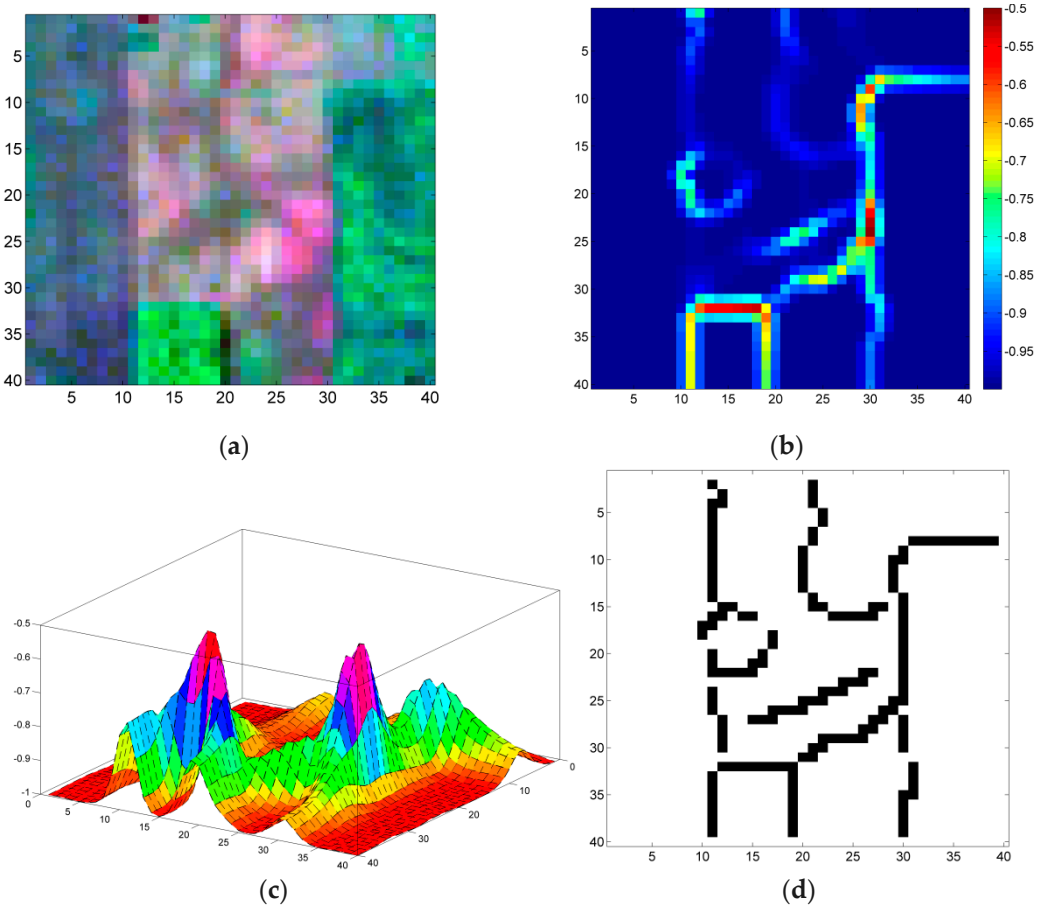

Figure 1. Illustration of the proposed approach. (**a**) A HSI with 224 bands, (**b**) Potential map of the HSI after applying a traveling operator, (**c**) Three-dimensional display of (b), (**d**) Final binarized and thinned edge map.

According to [3], a good detection should keep a thin and accurate localization of edges. To satisfy such requirements, information about edges' directions is necessary for non-maximum suppression. In accordance with [42], we first project the SPE to the horizontal and vertical directions in the spatial domain, as shown in Eq. (20).

$$\Phi_i^X = \sum_{j\in D} \varphi_{i,j} \cdot \frac{x_j}{\sqrt{(x_j + y_j)^2}} \quad \text{and} \quad \Phi_i^Y = \sum_{j\in D} \phi_{i,j} \cdot \frac{y_j}{\sqrt{(x_j + y_j)^2}}, \tag{20}$$

where Φ_i^X and Φ_i^Y are the SPE of pixel i projected onto the horizontal and vertical directions, respectively. Then, the edge direction is estimated by Eq. (21) as follows:

$$\theta_i = \arctan(\Phi_i^X / \Phi_i^Y). \tag{21}$$

With Φ and θ, non-maximum suppression and automatic hysteresis thresholding [45] can be applied to obtain the exact edge. As shown in Figure 1 (d), there is no spurious edge in the final result, and the detected edges can fully depict the main structure within the image.

The procedure of the GEDHSI algorithm is implemented in **Algorithm 1**, as illustrated in Table 1 as follows:

Table 1. Procedure of the GEDHSI algorithm.

Algorithm 1: GEDHSI

Mapping: Map pixels of HSI into a joint spatial-spectral feature space.

$\vec{Z}_i = (\vec{V}_i, \vec{S}_i) = (v_i^1, v_i^2 ..., v_i^b, \cdots, v_i^B, x_i, y_i)$ for i=1, 2, …, N.

Repeat until reaching the maximum number of iterations or minimum step size.

Traveling: For every pixel i, compose local dataset D following Eq. (13).

Calculate the resultant force and the inertial mass following Eq. (12) and Eq. (14).

Calculate the position update following Eq. (18).

SPE response:

Calculate the SPE response of each pixel with Eq. (19).

Obtain edge direction of each pixel with Eqs. (20) and (21).

Thinning and binarization.

4. Experiment Results and Discussions

To demonstrate the efficacy and efficiency of the proposed method, we carried out three groups of experimental validation, including quantitative and qualitative evaluation and CPU runtime. All edge results were compared between the proposed method and three other state-of-the-art multispectral edge detection methods, which include those from Di Zenzo [15], Drewniok [17] and RCMG [22]. Di Zenzo initially used the Sobel operator as channel-wise gradient technique [15], which is sensitive to noise. To improve the anti-noise anility, we prefer to use the ANDD--based gradient [46] considering its superiority in noise robustness. It is worth noting that the implementation codes of the comparative methods are directly taken from the authors for fair and consistent comparison. We selected their optimized parameters by trial-error methods. The parameters of GEDHSI were set as $h = 4$ and $\delta = 50$ in this paper. All the experiments were conducted under the following settings: Matlab2013a, 64 bit Windows 7 system, 2.9 GHz Intel Pentium CPU with 6 GB RAM.

Six hyperspectral data sets in three groups that include two artificial ones and four real natural scenes are used in our experiments for performance assessment as listed in Table 2. The artificial images contain two kinds of images, which were used to evaluate the performance in dealing with background clutter and weak edges. The real HSIs include two remote sensing HSIs and two ground scene HSIs. All these images are suitable to evaluate the performance of connectivity, edge resolution and the ability to suppress false edges.

Table 2. Properties of the data sets used in experiments.

	Data sets	Data source	Characteristic	Spatial Resolution	No. of Bands	Size (pixels)
1	AI 1	Artificial	background clutter	N/A	224	180×180
2	AI 2		weak edge, spectral mixture		224	180×180
3	Farmland	Remote sensing	straight lined boundary, textured	High	224	400×200
4	Washington DC Mall		many tiny objects, cluttered		191	466×307
5	Foster's Scene 5	Ground scene	man-made objects, textured wall, desk, ball, blocks etc.	Very high	31	820×820
6	Foster's Scene 7		textured wall, grass, shadow, etc.		31	690×425

Most edge detection techniques utilize thinning and binarization to obtain the final edge results [47]. In this study, we put all these edge strength maps into the same thinning process. In this process, a pixel is only considered as an edge if it is a local maximum in the horizontal or vertical direction.

Then, we applied the automatic threshold selection and hysteresis thresholding technique [45] on the edge strength maps to generate the binary edges.

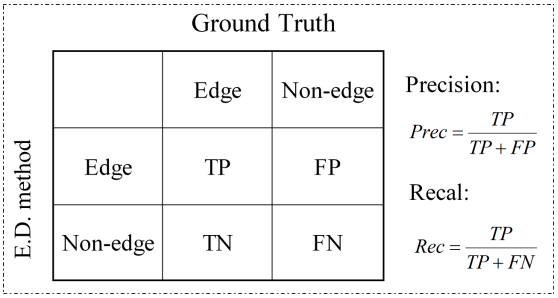

Figure. 2 Confusion matrix for the edge detection problem.

We investigated edge detection results with both subjective and quantitative evaluations. For quantitative evaluation, as shown in Figure 2, pixels in the candidate edge image were classified as TP (True Positive), TN (True Negative), FP (False Positive) and FN (False Negative), from which the precision and recall could be obtained as *Prec* and *Rec*. According to [23], the F-measure derived from *Prec* and *Rec* is used to evaluate the overall performance.

$$F_\alpha = \frac{Prec \times Rec}{\alpha \cdot Prec + (1\text{-}\alpha) \cdot Rec}, \tag{22}$$

where $\alpha \in [0,1]$ is a parameter weighing the contributions of *Prec* and *Rec*. In this paper, α was set to 0.5 to balance the *Prec* and *Rec*. As a statistical error measure, F-measure works well for false positive (FP) and false negative (FN), where a good detection has higher F-measure value.

In the rest of this section, we conducted three groups of experiments to test the performance of the proposed approach. Group 1 was employed to determinate the parameters of the GEDHSI. Group 2 was designed to quantitatively compare the performances of different edge detectors by using two artificial images, AI 1 and AI 2, which were embedded by background clutter or weak edges under different levels of noise. Group 3 was designed to validate the performance of the proposed approach on real remote sensing HSIs and ground scene HSIs. They were described in the following three subsections.

4.1 Evaluation on Artificial Datasets

In practice, there are two cases that make edge detection a challenge. The first one is objects that are embedded by background clutter, and the second is weak edges caused by spectral mixture or just appearing in a small subset of bands. As a result, we constructed two artificial images, AI 1 and AI 2, to evaluate the performance of our proposed edge detection approach under these two cases.

A. Experiment on AI 1

In this experiment, we investigated the behaviors of the four edge-detection methods when the objects in an image are embedded by background clutter. We first synthesized the artificial image AI 1 using HYDRA [48], which has a spatial dimension of 180×180 in 224 bands. AI 1 is composed of one object (in the middle) and a background, where the object is located between column 60 and column 120. Thus, edge pixels are located at columns 60 and 120. To simulate different levels of background clutter, we added Gaussian noises with various Signal Noise Ratio (SNR) to AI 1. The object noise is fixed to SNR=16 dB, whereas the background noise varies from 0.1 to 3.0 dB. Figure 3 (a) shows the content of the synthetic image without noise. Figure 3 (b) shows a channel for the background with SNR=0.2 dB.

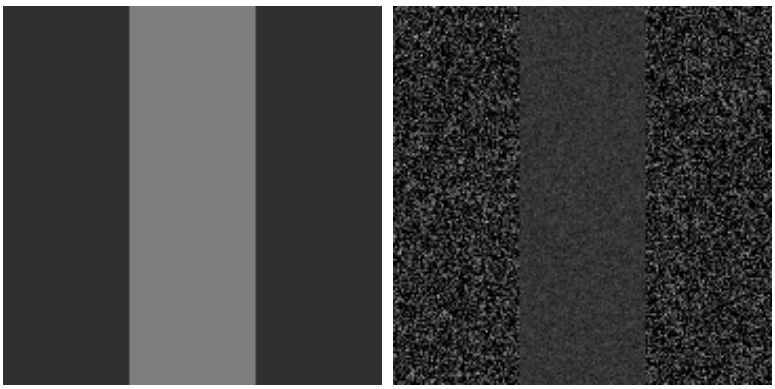

(**a**) (**b**)

Figure 3. A channel in the AI 1 dataset. (**a**) The content of the synthetic image without noise (object is located in the middle) and (**b**) a corrupted image with SNR=16 dB in the object region and SNR=0.2 dB in the background region. The dark color indicates low intensity.

Figure 4 shows an edge-detection example for AI 1, where the background noise is SNR=0.2 dB. The edge-strength maps and corresponding binary edge maps were shown in the first row and the second row, respectively, in Figure 4. For Di Zenzo's method, the strength of the edge pixels is slightly larger than the background (Figure 4 (b)). Although we can set a pair of thresholds to separate edge and non-edge pixels, severe false positive detections cannot be avoided, as shown in Figure 4 (f). For the RCMG, the strength of noisy pixels is larger than that of edge pixels, as shown in Figure 4 (c); thus, the boundaries of the object were concealed from the noisy background (Figure 4 (g)). According to Figure 4 (d) and Figure 4 (h), the results of Drewniok's method are better than those of Di Zenzo's and the RCMG method, but they blurred the edges to some extent (Figure 4 (d)). Therefore, the object's edges were blurred with burrs, as shown in Figure 4 (h). Compared to the other three methods, the better performance of the presented detector is clearly perceivable, and the strength of the edge pixels is larger than that of the noise pixels (Figure 4 (a)). It is therefore easy to set appropriate thresholds to separate the edge and non-edge pixels, as shown in Figure 4 (e).

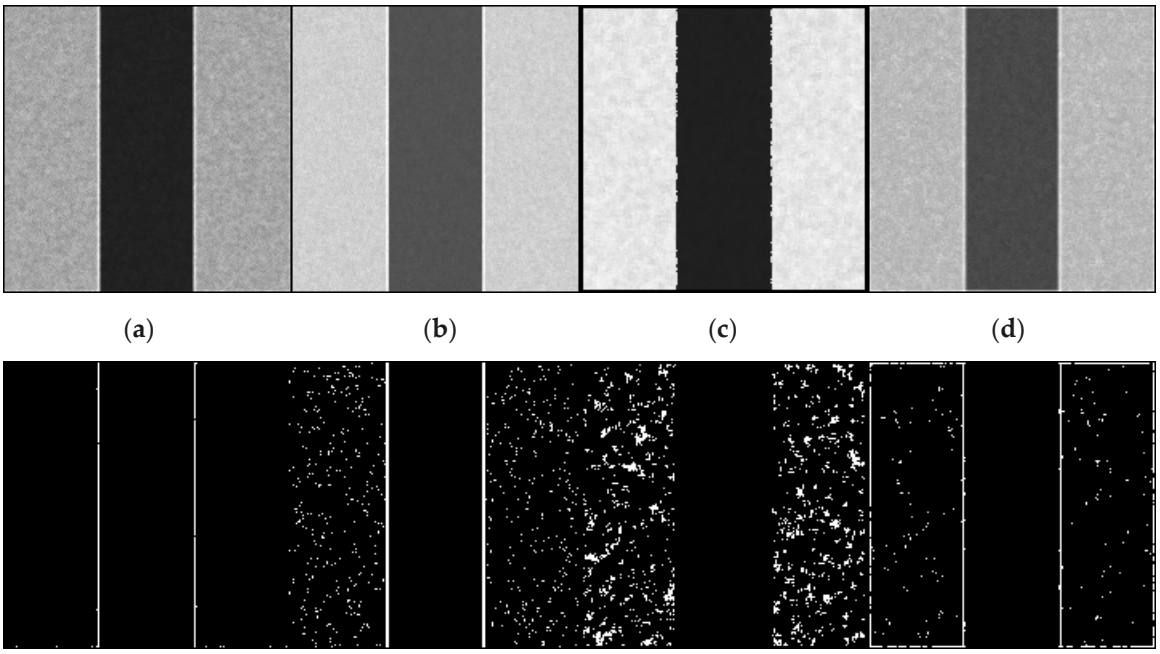

(**a**) (**b**) (**c**) (**d**)

(**e**) (**f**) (**g**) (**h**)

Figure 4. Edge-strength maps and corresponding binary edges of AI 1 with SNR=0.2 dB. Edge-strength maps of (**a**) GEDHSI, (**b**) Di Zenzo's method, (**c**) the RCMG method and (**d**) Drewniok's method. (**e**)-(**h**) Binary edge maps of corresponding results of (a)-(d).

The robustness to the background clutter of the GEDHSI was further demonstrated in Figure 5, using performance evaluation results of the four methods under a background-noise level from 0.1 to 3 dB. From Figure 5 we could find that under high background-noise levels (SNR approximately 0.1 dB), the GEDHSI produced an F-measure value larger than 0.9, whereas the F-measure values produced by Di Zenzo's method and the RCMG are both smaller than 0.6. The F-measure value of Drewniok's method is near 0.8 but still much less than that of the GEDHSI. As SNR being increased to above 0.9, the F-measure value for GEDHSI reaches approximately 1.0, whereas the F-measure values for Di Zenzo's methods, the RCMG and Drewniok's method increase slowly. It is obvious that the other three methods are inferior to the GEDHSI in addressing such severe background clutter. With severe noise interference, the large difference between a noisy pixel and its neighbors usually led to a high gradient magnitude for the noisy pixel, a magnitude that is even larger than the gradient magnitudes of the true edge pixels. As a result, they will inevitably cause incorrect results because they fail to make the full use of the spatial information of the image, especially less consideration to the relationships of pixels within a local window.

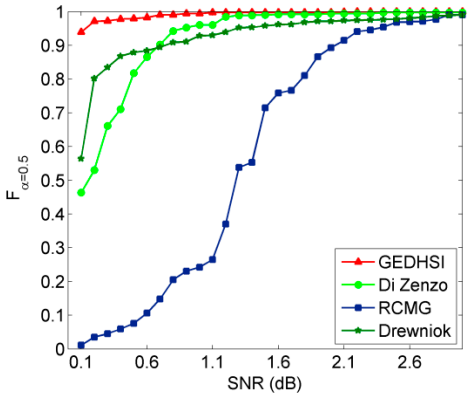

Figure 5. Performance evaluation on AI 1 under various noise levels.

B. Experiment on AI 2

In this experiment, we analyze the behaviors of the four edge-detection methods in dealing with weak edges between objects. For HSIs, weak edges are usually caused by spectral mixture between objects or edges appearing in only a small subset of bands [13, 25]. To tackle this problem, we generated a well-designed image AI 2 with a spatial dimension of 180×180 in 9 regions. The size of each region is 60×60 pixels. We first selected three types of endmembers from the USGS Spectral Library [49], as shown in Figure 6 (a).

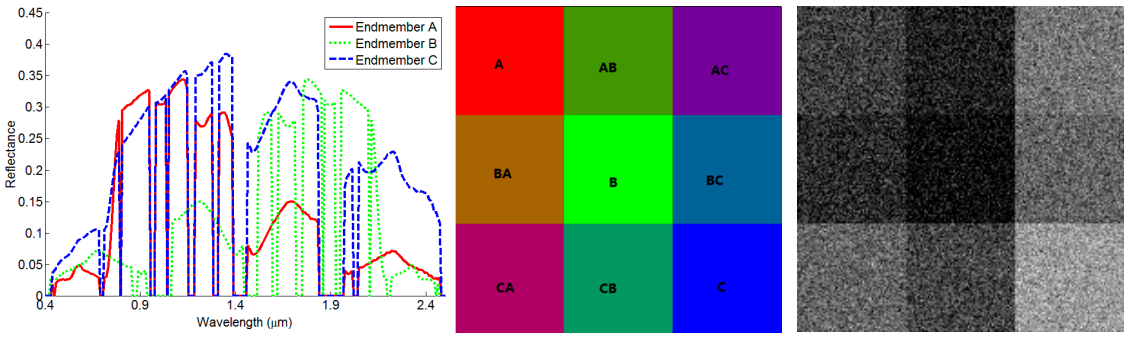

(**a**) (**b**) (**c**)

Figure 6. Materials for AI 2, (**a**) curve of endmembers, (**b**) diagram of AI 2 and (**c**) a band of AI 2 with SNR=10 dB.

According to Figure 6 (a), the two endmembers A and C are found to be very similar in the range of 0.6μm to 1.4μm; whereas the two endmembers B and C are very similar in the range of 1.5μm to 2.1μm. A diagram of AI 2 is shown in Figure 6 (b), where the symbol of each region

denotes which endmembers the region is formed. For example, the "A" of Region A means the region was generated only using endmember A, Region AB was generated by using endmembers A and B, whereas Region BA was composed of endmembers B and A et al. Except for the three regions located in the principal diagonal, all regions were mixed by different endmembers. The mixed ratio was fixed as 0.4:0.6 for these regions. We then added Gaussian noise to AI 2 and result in a varying SNR between 1 and 30 dB. Figure 6 (c) shows an example band with SNR=10 dB. Due to the spectral mixture and spectral similarity in many bands, there are several weak edges. Under such conditions, weak edges may be easily vanished in noise when white Gaussian noise was added.

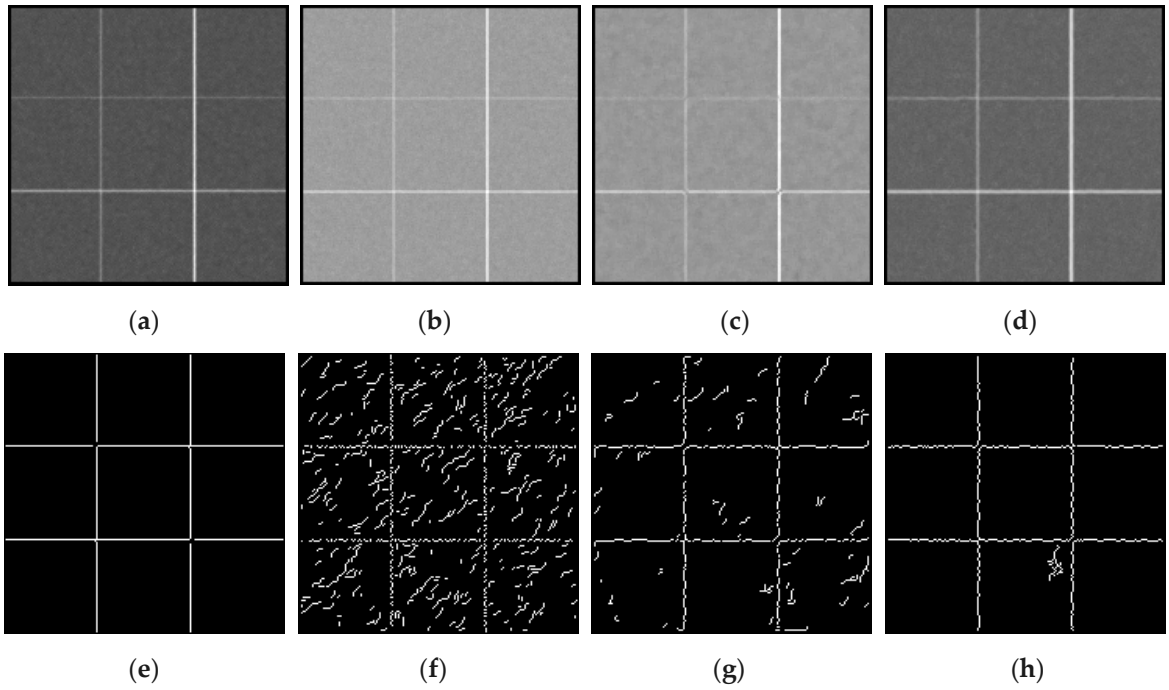

Figure 7. Edge-strength maps and corresponding binary edges of AI 2 with SNR=10 dB. Edge-strength maps of (**a**) GEDHSI, (**b**) Di Zenzo's method, (**c**) the RCMG method and (**d**) Drewniok's method. (**e**)-(h) Binary edge maps of corresponding results of (a)-(d) by applying automatic hysteresis thresholding and thinning processes.

For the noise-degraded AI 2 with a SNR of 10 dB, Figure 7 shows the edge-strength maps (the first row) and their corresponding binary edge maps (the second row) generated by the four methods. As seen from the edge-strength maps generated by Di Zenzo's method (Figure 7 (b)), the RCMG (Figure 7 (c)) and Drewniok's method (Figure 7 (d)), the strength of upper horizontal and left vertical edge pixels is close to that of the noisy pixels. Therefore, it is difficult to set appropriate thresholds for these edge-strength maps. According to Figure 7 (f)-(g), Di Zenzo's method seems to produce discontinuous edges and severe false edges. The RCMG is slightly better but still contains some spurious edges. Although Drewniok's method has removed almost all noise, the edges are hackly due to the displacement caused by Gaussian smoothing in each band. For comparison, the intensity of the edge pixels is dramatically larger than that of the noisy pixels, as shown in Figure 7 (a). Thus, thresholding can easily classify edge and non-edge pixels, as shown in Figure 7 (e).

Figure 8 shows the performance comparison of the four methods under noise from 1.0 to 30 dB. As seen, there were two critical points for each curve: the start point, where SNR=1.0 dB, and the stable point, where the F-measure value reaches the maximum. GEDHSI has the highest F-measure value at the starting point. The stable point of GEDHSI is SNR=10 dB where we have F_α=0.98, while the other three methods reach stable points at SNR=15 dB. To this end, we can draw a conclusion that GEDHSI is markedly more robust to severe noise and weak edges than the other three methods.

Preprints (www.preprints.org) | NOT PEER-REVIEWED | Posted: 19 May 2017 doi:10.20944/preprints201705.0142.v1

Peer-reviewed version available at Remote Sens. 2017, 9, , 592; doi:10.3390/rs9060592

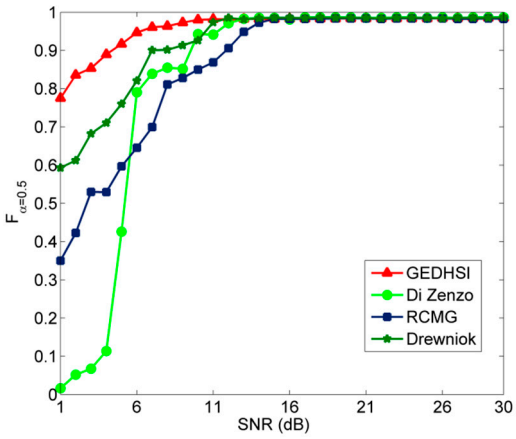

Figure 8. Performance evaluation on AI 2 under various noise levels.

4.2 Evaluation on Real World Datasets

4.2.1 Experiments on Remote Densing Datasets

For remote sensing images, due to the complexity of land cover based surface feature, illumination and atmospheric effects as well as spectral mixing of pixels, edges are always deteriorated for proper detection. More seriously, there usually exist some noisy bands in remote sensing HSIs, which make edge detection very difficult. To validate the performance of edge detection on remote sensing HSIs, we selected two remote sensing HSIs, the Farmland and Washington DC Mall image, to conduct experiments in this section.

A. Experiment on the Farmland HSIs

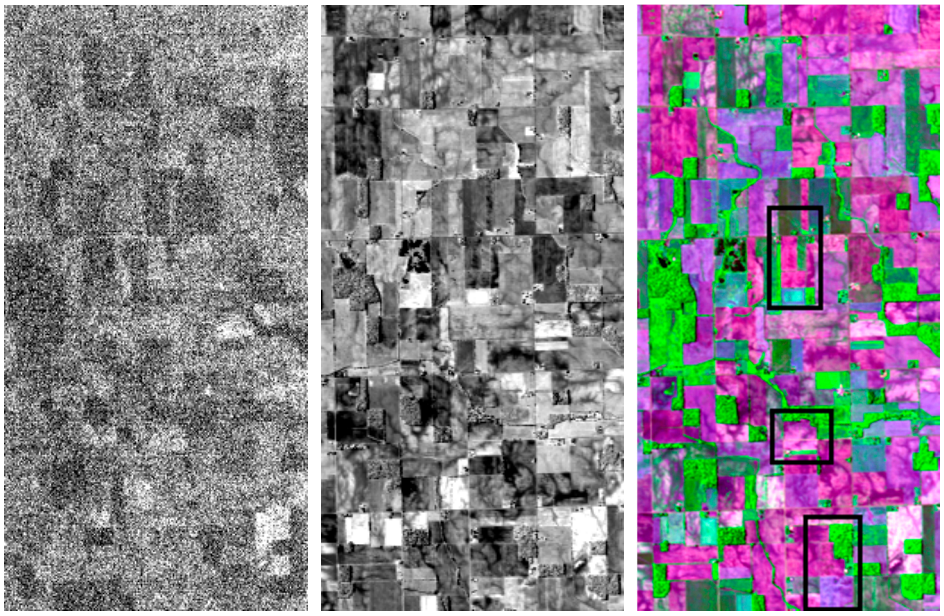

(**a**) (**b**) (**c**)

Figure 9. Farmland image. (a) Noisy image in gray-scale (band 1), (b) Noiseless image in gray-scale (band 87), (c) Three-band false color composite (bands 25, 60, 128).

Figure 9 is an AVIRIS flight line over a farmland of east-central Indiana [50]. The AVIRIS instrument contains 224 different detectors, where the spectral band width is approximately 0.01 μm, allowing it to cover the entire range between 0.4 μm and 2.5 μm. There are several low SNR bands in AVIRIS image, and one example is shown in Figure 9 (a) where the edges are nearly

invisible. Even in some noiseless band as shown in Figure 9 (b) the edges are still very vague. Composited with three low correlation bands, the edge structure can be much clearer as shown in Figure 9 (c). This is mainly results from more spectral information is used. Due to the composited image has clear and straight lined boundary between regions, it is appropriate for performance evaluation. However, in the composited image, the pixels inside the region are heavily textured, which makes edge detection a difficult problem.

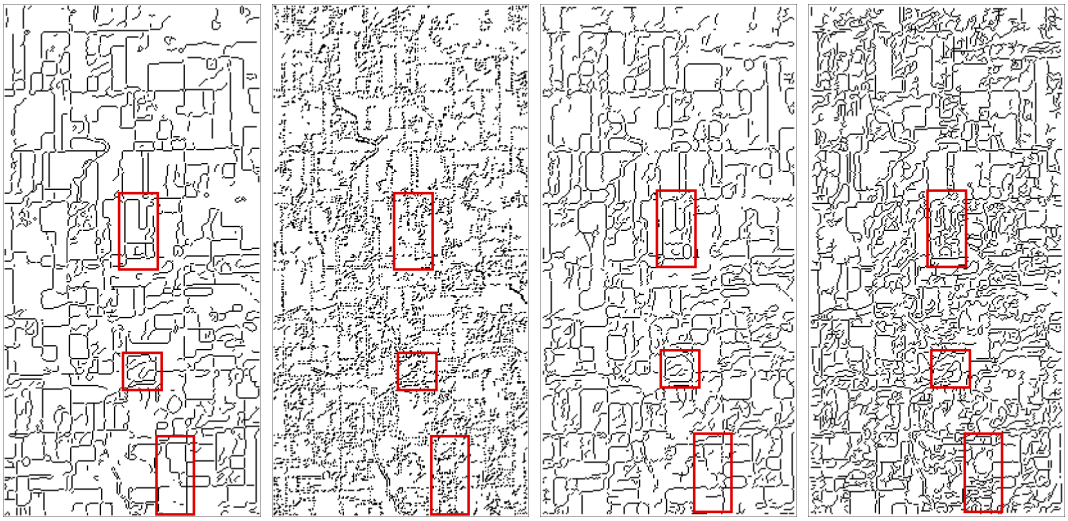

(**a**) (**b**) (**c**) (**d**)

Figure 10. The binary edge maps of the Farmland image by (a) GEDHSI, (b) Di Zenzo's method, (c) the RCMG method and (d) Drewniok's method ($\sigma = 1.0$) .

Figure 10 illustrates the results of edge detection from the four methods. Overall, the better performance of the GEDHSI on the image is clearly perceivable. The proposed GEDHSI has produced continuous, compact and clear edges, where the most edge structures are well preserved as shown in Figure 10 (a). For Di Zenzo's method, almost all of edges produced are broken as shown in Figure 10 (b). Drewniok's method generates many spurious edges within regions and some line edges are distorted at the place where it should be straight according to Figure 10 (d). Although the RCMG yields similar edges as GEDHSI, there are many grainy edges with some fine edge structures missing or distorted to some degree as shown in Figure 10 (c). Specifically, as labeled by the red rectangles, Di Zenzo's method has detected serious broken edges. Drewniok's method generates many small and severe spurious edges and fails to capture the main structure. What's more, Drewniok's method results in distortion and flexuous edges. The RCMG produces some grainy and slightly distorted edges. In contrast, the edges produced by the proposed GEDHSI are straight and continuous.

B. Experiment on the Washington DC Mall HSIs

Figure 11 is an airborne hyperspectral data flight line over the Washington DC Mall [51], which has 210 bands ranging from 0.4 μm to 2.4 μm and covers the visible and (near) infrared spectrum. Bands in the 0.9 μm and 1.4 μm regions where the atmosphere is opaque have been omitted from the dataset, leaving 191 bands for experiments. As shown in Figure 11 (a), the dataset contains complex and cluttered landcovers. Especially, in the middle of Figure 11 (a) as highlighted within a doted rectangle, various roofs, roads, trails, grass, trees and shadow are cluttered. For better visual effect, the enlarged version of this part of the image is shown in Figure 11 (b). This is used for testing as it contains abundant tinny edges which is difficult to be detected completely. Examples of these tiny structures can be found in the two ellipses in Figure 11 (b), where local details such as the boxes on the roof and the footpath are clearly visible yet hard for detection.

Preprints (www.preprints.org) | NOT PEER-REVIEWED | Posted: 19 May 2017 doi:10.20944/preprints201705.0142.v1

Peer-reviewed version available at Remote Sens. 2017, 9, , 592; doi:10.3390/rs9060592

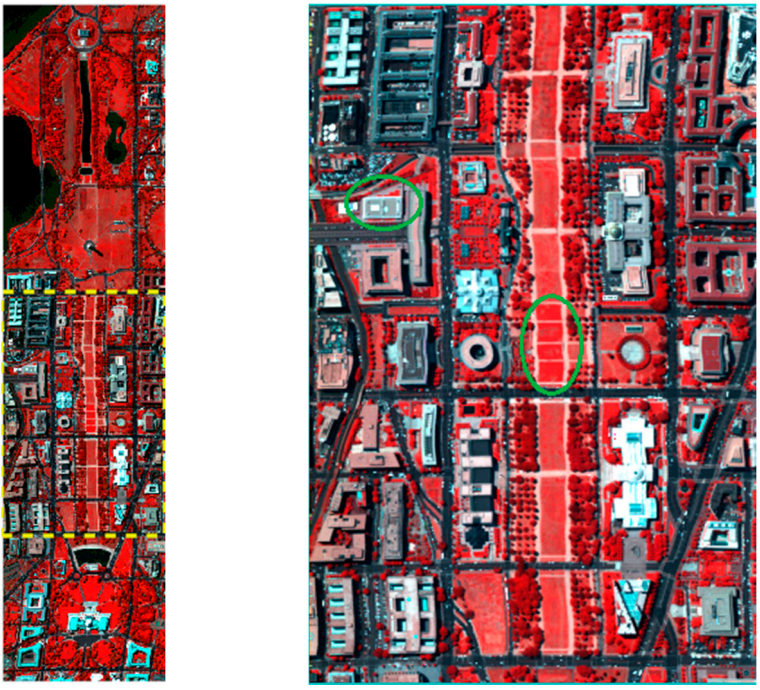

(**a**) (**b**)

Figure 11. False color representation of the Washington DC Mall hyperspectral data. (**a**) The whole data, (**b**) The detail display of the doted rectangle region of (a) with two regions emphasized in ellipses to show local tiny structures.

Figure 12 illustrates the edge results for Figure 11 (b) produced by the four methods. According to the criteria of reference [46], a good detection should keep good edge resolution and connectivity. The superiority of the proposed method on these criteria is clearly visible as shown in Figure 12. The edge image of Di Zenzo's method is poor and contains many broken edges as shown in Figure 12 (b). The RCMG is better than Di Zenzo's method, but it still produces many grainy and spurious edges (Figure 12 (c)). Compared with Figure 12 (c), the edge map produced by the Drewniok's method in Figure 12 (d) contains more grainy edges within regions and more spurious edges. In contrast, the edges in Figure 12 (a) produced by our approach are clearer and of better connectivity, where most of fine edge structures from different land covers are successfully detected.

(**a**) (**b**) (**c**) (**d**)

Figure 12. The binary edge maps of the Washington DC Mall by (a) GEDHSI, (b) Di Zenzo's method, (c) the RCMG method, (d) Drewniok's method (σ =1.0).

For the edge resolution criterion, the better performance of the proposed method is also obviously perceivable. In the upper left ellipse of Figure 12 (b), the RCMG and Di Zenzo's method

have missed the edge structures, while the proposed GEDHSI preserve well such tiny structures. In the lower right corner ellipse of Figure 12 (c) and Figure 12 (d), The RCMG and Drewniok's method not only fail to obtain continuous edge but also miss one side of the edge. On the contrary, the proposed GEDHSI can detect complete edges at both side of the path. On the whole, the proposed approach is more effective than the other three methods for detecting edges from these HSIs.

4.2.2 Experiments on Ground Scene Datasets

To further investigate the performance of the proposed method on real ground scenes, we considered the Foster's HSI dataset [52]. The images of the dataset cover the wavelength from 0.4 μm to 0.72 μm, and are sampled at 0.01 μm intervals and result in 31 bands. For simplicity, we selected two images, Scenes 5 and Scenes 7 as illustrated, because of the following two reasons: First, as shown in Figure 13, the spatial resolution is higher than the other 4 datasets and they contain many man-made objects, thus we know where the edges occur exactly. Therefore, they are rather appropriate for performance evaluation. Second, there are heavily textured objects in the datasets, such as the objects surrounded by a heavily textured wall in Scene 5 (Figure 13 (a)), and finely textured walls and grass in Scene 7 (Figure 13 (b)). Edge detection under these circumstance is still a challenging.

(**a**) (**b**)

Figure 13. RGB representations of two hyperspectral scene dataset. (**a**) Scene 5, (**b**) Scene 7.

A. Experiment on the Scene 5 dataset

For the Scene 5 dataset, Figure 14 illustrates the binary edge maps generated by the four methods. Obviously, Di Zenzo's edge image is poor and contains many small and spurious edges, and the details of the wall are poorly detected as shown in Figure 14 (b). Compared to Figure 14 (b), the RCMG method can detect more edges on the wall, while there are still some spurious edges especially on the chair, under the ball and at the bottom right of the wall due to the variance in intensity of the surface as shown in Figure 14 (c). Drewniok's method performs better than Di Zenzo's method on the wall, but it has produced more spurious and grainy edges than either the RCMG or GEDHSI. Some fine edges on the wall grid and racket bag are missing (Figure 14 (d)). In contrast, almost complete edges of most objects are attained by the proposed method as shown in Figure 14 (a). The details in the circle from Figure 14 also illustrate the efficacy of the proposed method, where the proposed GEDHSI method has generated the best edge results in keeping the real structure.

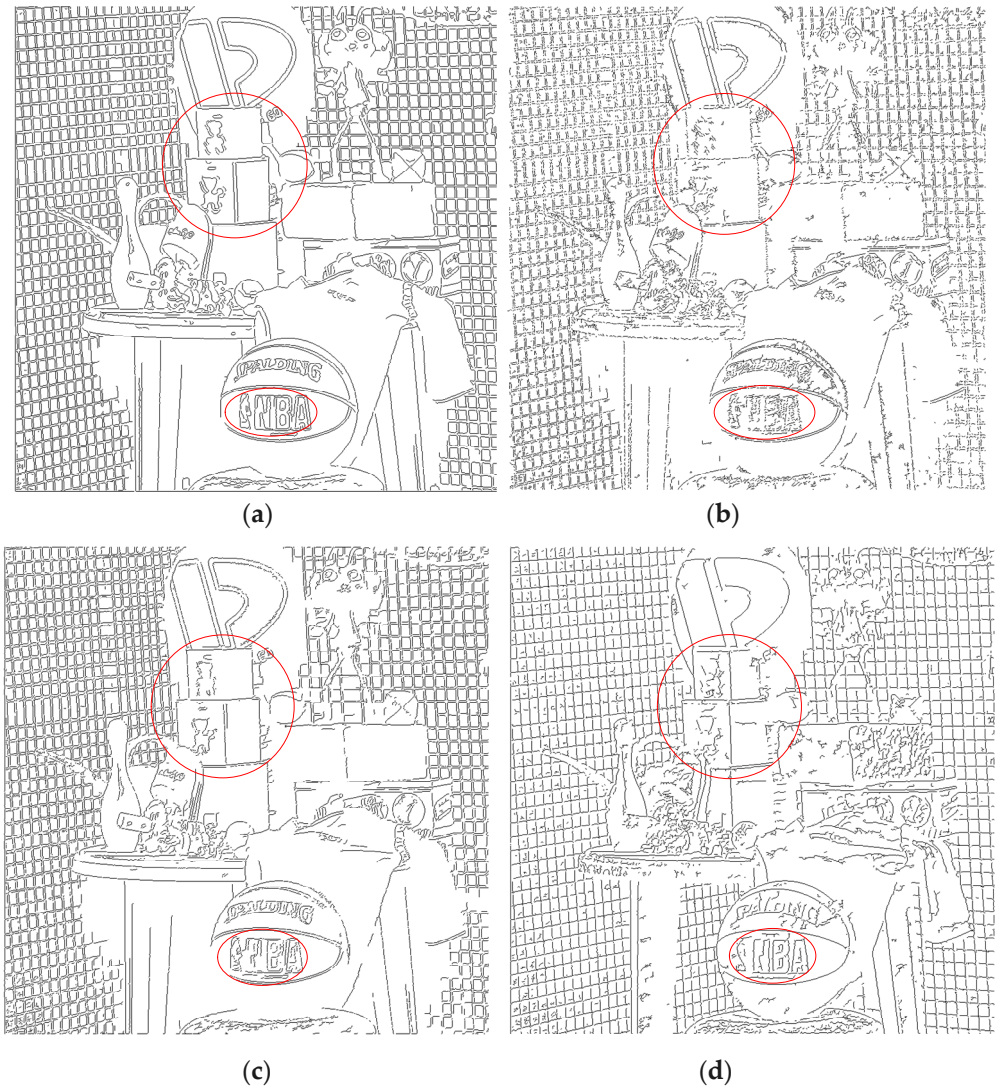

Figure 14. The binary edge maps generated for the Scene 5 dataset by (**a**) GEDHSI, (**b**) Di Zenzo's method, (**c**) the RCMG method and (**d**) Drewniok's method (σ =1.0) .

B. Experiment on Scene 7

Figure 15 shows the binary edge maps of Scene 7 produced by the four methods. Accoding to Figure 15 (b), Di Zenzo's method produces many spurious edges and performes poorly on connectivity. The RCMG preserves most significant spatial structures, but it also brings many grainy edges especially in the grass region. The Drewniok's method can detect many edges on the wall and grass, but the interval between edges on the windows is enlarged due to edges displacement caused by Gaussian smoothing. Comparatively, the better performance of the proposed method is perceivable. Most of fine edge structures such as the edges located at the windows are attained and the edges are clear and connective as shown in Figure 15 (a). More specifically, as indicated by the circle at the bottom of the image, Di Zenzo's and Drewniok's methods produce undesirable edges for the grass in the circle. The RCMG almost misses the edge structure. Comparatively, the fine structure is well perserved by the proposed GEDHSI method. At the right bottom ellipse, Drewniok's method has missed both the edge of the left sidewalls and the edge between the middle white door and the dark shadow. On the contrary, the proposed GEDHSI can again detect correct edges without missing main structure of that region.

Preprints (www.preprints.org) | NOT PEER-REVIEWED | Posted: 19 May 2017 doi:10.20944/preprints201705.0142.v1

Peer-reviewed version available at Remote Sens. 2017, 9, , 592; doi:10.3390/rs9060592

(a) (b) (c) (d)

Figure 15. The binary edge maps generated for the Scene 7 by (a) GEDHSI, (b) Di Zenzo's method, (c) the RCMG method and (d) Drewniok's method (σ =1.0) .

On the whole, three groups of comparative experiments above have validated the superiority of the proposed GEDHSI for edge detection in HSIs. The proposed method is more robust to background clusters and weak edges, as illustrated by the experiments on artificial images. For real-world images, it is robust to noisy bands in keeping complete and reasonable spatial structures and performs well on edge localization and resolution. As a result, GEDHSI is more suitable for HSI edge detection than other state-of-the-art multi-band approaches.

4.3 Comparison of Runtime

In this section, we compare the computational efficiency of the above four algorithms. The mean computational time (in seconds) required by each algorithm for 5 independent runs in solving the 2 tested images, the Farmland and Washington DC Mall, are presented for comparison.

Table 3. The time efficiency evaluation.

Image	GEDHSI	Di Zenzo	RCMG	Drewniok
Farmland	32.17s	15.65s	4.04s	13.55s
Washington DC Mall	36.56s	22.45s	4.81s	14.28s

As seen in Table 3, RCMG takes the least time, and one main reason is its C++ based implementation in comparison to Matlab-based implementation for the other three methods. The proposed GEDHSI, unfortunately, consumes the longest runtime as a whole. The long time consuming is largely caused by the iterative computation in travelling procedure. For each particle, the repeating calculation of gravitational force for all particles in dataset *D* leads to heavy burden of runtime. How to speed up the process and improve the efficiency of GEDHSI will be investigated in the future.

5. Conclusion

In recent years, various heuristic and physically inspired image-understanding methods have been developed. To extract the edges from HSIs, a novel edge-detection method, namely Gravitation-based Edge Detection on HSIs (GEDHSI), is presented in this paper. In GEDHSI, each pixel is assumed to be a movable celestial object in the spatial-spectral jointed feature space. Then, all objects travel in the feature space under the gravitational field force. Due to the relative positions, the edge and non-edge pixels can be separated by computing potential energy field. In addition to its simplicity and generality, GEDHSI has promising theoretical properties that make it an attractive tool for edge detection. The performance of the proposed algorithm has been compared with three state-of-the-art methods, including Di Zenzo's, Drewniok's and RCMG detectors. Experiments on a variety of datasets have validated the efficacy of the proposed algorithm in effective edge-detection

for HSIs. In the future, we will focus on further improving the efficiency of the approach and also investigating the relationship between the edge scale and the scale parameters for improved edge results in the scale space.

Acknowledgments: This work was supported by Chinese Natural Science Foundation Projects (41471353) and National Key Research and Development Program of China (2016YFB0501501).

Author Contributions: Genyun Sun, Aizhu Zhang, and Peng Wang conceived, designed and performed the experiments, analyzed the data, and wrote the paper; all authors reviewed the manuscript.

Conflicts of Interest: The authors declare no conflict of interest.

References

1. Tarabalka, Y.; Benediktsson, J.A.; Chanussot, J. Spectral–spatial classification of hyperspectral imagery based on partitional clustering techniques. *IEEE T. Geosci. Remote* **2009**, 47, 2973–2987.
2. Weng, Q.; Quattrochi, D.A. *Urban remote sensing*; CRC Press, 2006.
3. Canny, J. A computational approach to edge detection. *IEEE T. Pattern Anal.* **1986**, pp. 679–698.
4. Marr, D.; Hildreth, E. Theory of edge detection. Proceedings of the Royal Society of London, London, Great Britain, 29 Feb 1980; pp. 187-217.
5. S. M. Smith and J. M. Brady, SUSAN—a new approach to low level image processing. *Int. J. Comput. Vision* **1997**, *23*, 45-78.
6. Chan, T. F.; Vese, L. A. Active contours without edges. *IEEE T. Image. Process.* **2001**, *10*, 266-277.
7. Priego, B.; Souto, D.; Bellas, F.; Duro, R.J. Hyperspectral image segmentation through evolved cellular automata. *Pattern Recogn. Lett.* **2013**, *34*, 1648–1658.
8. Tarabalka, Y.; Chanussot, J.; Benediktsson, J.A. Segmentation and classification of hyperspectral images using watershed transformation. *Pattern Recogn.* **2010**, *43*, 2367–2379.
9. Bakker, W.; Schmidt, K. Hyperspectral edge filtering for measuring homogeneity of surface cover types. *ISPRS J. Photogramm.* **2002**, *56*, 246–256.
10. Kanade, T. Image understanding research at CMU. *Darpa Iuw* **1982**.
11. Hedley, M.; Yan, H. Segmentation of color images using spatial and color space information. *J. Electron. Imaging* **1992**, *1*, 374-380.
12. Fan, J.; Yau, D. K.; Elmagarmid, A. K.; Aref, W. G. Automatic image segmentation by integrating color-edge extraction and seeded region growing. *IEEE T. Image. Process.* **2001**, *10*, 1454-1466.
13. Garzelli, A.; Aiazzi, B.; Baronti, S.; Selva, M.; Alparone, L. Hyperspectral image fusion. Proceedings of the Hyperspectral 2010 Workshop, 2010, pp. 17–19.
14. Lei, T.; Fan, Y.;Wang, Y. Colour edge detection based on the fusion of hue component and principal component analysis. *IET Image Process.* **2014**, *8*, 44-55.
15. Di Zenzo, S. A note on the gradient of a multi-image. *LECT Notes. Comput. Sc.* **1986**, *33*, 116–125.
16. Cumani, A. Edge detection in multispectral images. *CVGIP-Graph. Model. Im.* **1991**, *53*, 40–51.
17. Drewniok, C. Multi-spectral edge detection. Some experiments on data from Landsat-TM. *Int. J. Remote Sens.* **1994**, *15*, 3743–3765.
18. Jin, L.; Liu, H.; Xu, X.; Song, E. Improved direction estimation for Di Zenzo's multichannel image gradient operator. *Pattern Recogn.* **2012**, *45*, 4300–4311.
19. Trahanias, P.E.; Venetsanopoulos, A.N. Color edge detection using vector order statistics. *IEEE T. Image. Process.* **1993**, *2*, 259–264.
20. Toivanen, P. J.; Ansamäki, J.; Parkkinen, J.; Mielikäinen, J. Edge detection in multispectral images using the self-organizing map. *Pattern Recogn. Lett.* **2003**, *24*, 2987-2994.
21. Haralick, R.M.; Sternberg, S.R.; Zhuang, X. Image analysis using mathematical morphology. *IEEE T. Pattern. Anal.* **1987**, pp. 532–550.
22. Evans, A.N.; Liu, X.U. A morphological gradient approach to color edge detection. *IEEE T. Image. Process.* **2006**, *15*, 1454–1463.
23. Lopez-Molina, C.; De Baets, B.; Bustince, H. Quantitative error measures for edge detection. *Pattern Recogn.* **2013**, *46*, 1125–1139.
24. Wang, Y.; Niu, R.; Yu, X. Anisotropic diffusion for hyperspectral imagery enhancement. *IEEE Sens. J.*, **2010**, *10*, 469-477.

25. Dinh, C.V.; Leitner, R.; Paclik, P.; Loog, M.; Duin, R.P. SEDMI: Saliency based edge detection in multispectral images. *Image Vision Comput.* **2011**, *29*, 546–556.
26. Paskaleva, B.S.; Godoy, S.E.; Jang, W.Y.; Bender, S.C.; Krishna, S.; Hayat, M.M. Model-Based Edge Detector for Spectral Imagery Using Sparse Spatiospectral Masks. *IEEE T. Image. Process.* **2014**, *23*, 2315–2327.
27. Lin, Z.; Jiang, J.; Wang, Z. Edge detection in the feature space. *Image Vision Comput.* **2011**, *29*, 142–154.
28. Jia, X.; Richards, J.; others. Cluster-space representation for hyperspectral data classification. *IEEE T. Geosci. Remote* **2002**, *40*, 593–598.
29. Imani, M.; Ghassemian, H. Feature space discriminant analysis for hyperspectral data feature reduction. *ISPRS J. Photogramm.* **2015**, *102*, 1–13.
30. Gomez-Chova, L.; Calpe, J.; Camps-Valls, G.; Martin, J.; Soria, E.; Vila, J.; Alonso-Chorda, L.; Moreno, J. Feature selection of hyperspectral data through local correlation and SFFS for crop classification. Geoscience and Remote Sensing Symposium, 2003. IGARSS'03. Proceedings. 2003 IEEE International. IEEE, 2003, Vol. 1, pp. 555–557.
31. Rashedi, E.; Nezamabadi-Pour, H. A stochastic gravitational approach to feature based color image segmentation. *Eng. Appl. Artif. Intel.* **2013**, *26*, 1322–1332.
32. Sen, D.; Pal, S. K. Improving feature space based image segmentation via density modification, *Inform. Sciences* **2012**, *191*, 169-191.
33. Peters, R. A. A new algorithm for image noise reduction using mathematical morphology. *IEEE T. Image. Process.* **1995**, *4*, 554-568.
34. Perona, P.; Malik, J. Scale-space and edge detection using anisotropic diffusion. *IEEE T. Pattern Anal.* **1990**, *12*, 629–639.
35. Olenick, R.P.; Apostol, T.M.; Goodstein, D.L. *The Mechanical Universe: Introduction to Mechanics and Heat*; Cambridge University Press, 2008.
36. de Mesquita Sá Junior, J. J.; Ricardo Backes, A.; César Cortez P. Color texture classification based on gravitational collapse, *Pattern Recogn.* **2013**, *46*, 1628-1637.
37. Peng, L.; Yang, B.; Chen, Y.; Abraham, A. Data gravitation based classification. *Inform. Sciences* **2009**, *179*, 809–819.
38. Cano, A.; Zafra, A.; Ventura, S. Weighted data gravitation classification for standard and imbalanced data. *IEEE T. Cyb.* **2013**, *43*, 1672–1687.
39. Peng, L.; Zhang, H.; Yang, B.; Chen, Y. A new approach for imbalanced data classification based on data gravitation. *Inform. Sciences* **2014**, *288*, 347–373.
40. Ilc, N.; Dobnikar, A. Generation of a clustering ensemble based on a gravitational self-organising map. *Neurocomputing* **2012**, *96*, 47–56.
41. Lopez-Molina, C.; Bustince, H.; Fernández, J.; Couto, P.; De Baets, B. A gravitational approach to edge detection based on triangular norms. *Pattern Recogn.* **2010**, *43*, 3730–3741.
42. Sun, G.; Liu, Q.; Liu, Q.; Ji, C.; Li, X. A novel approach for edge detection based on the theory of universal gravity. *Pattern Recogn.* **2007**, *40*, 2766–2775.
43. Hulthén, L.; Sugawara, M. Encyclopaedia of Physics, 39, 1957.
44. Rashedi, E.; Nezamabadi-Pour, H.; Saryazdi, S.; GSA: a gravitational search algorithm, *Inform. sciences* **2009**, 179, 2232-2248.
45. Medina-Carnicer, R.; Munoz-Salinas, R.; Yeguas-Bolivar, E.; Diaz-Mas, L. A novel method to look for the hysteresis thresholds for the Canny edge detector. *Pattern Recogn.* **2011**, *44*, 1201–1211.
46. Shui, P.L.; Zhang,W.C. Noise-robust edge detector combining isotropic and anisotropic Gaussian kernels. *Pattern Recogn.n* **2012**, *45*, 806–820.
47. González-Hidalgo, M.; Massanet, S.; Mir, A.; Ruiz-Aguilera, D. On the pair uninorm-implication in the morphological gradient. In Computational Intelligence; K. Madani; A. D. Correia; A. Rosa; J. Filipe; Springer International Publishing: Cham, Switzerland, 2015; Volume 577, pp. 183-197.
48. Rink, T.; Antonelli, P.; Whittaker, T.; Baggett, K.; Gumley, L.; Huang, A.; others. Introducing HYDRA: A multispectral data analysis toolkit. *B. Am. Meteorol. Soc.* **2007**, *88*, 159-166.
49. Clark, R.N.; Swayze, G.A.; Wise, R.; Livo, K.E.; Hoefen, T.M.; Kokaly, R.F.; Sutley, S.J. USGS digital spectral library splib06a, 2007.

50. Green, R.O.; Eastwood, M.L.; Sarture, C.M.; Chrien, T.G.; Aronsson, M.; Chippendale, B.J.; Faust, J.A.; Pavri, B.E.; Chovit, C.J.; Solis, M.; others. Imaging spectroscopy and the airborne visible/infrared imaging spectrometer (AVIRIS). *Remote Sens. Environ.* **1998**, *65*, 227–248.
51. Landgrebe, D. Hyperspectral image data analysis. *IEEE Signal. Proc. Mag.* **2002**, *19*, 17–28.
52. D. H. Foster. Hyperspectral Images of Natural Scenes 2002. Available online: http://personalpages.manchester.ac.uk/staff/david.foster/2002